

Spline-Shaped Microstrip Edge-Fed Antenna for 77 GHz Automotive Radar Systems

M. Salucci,⁽¹⁾ *Senior Member, IEEE*, L. Poli,⁽¹⁾ *Member, IEEE*, P. Rocca,⁽¹⁾⁽²⁾ *Senior Member, IEEE*, C. Massagrande,⁽³⁾ P. Rosatti,⁽¹⁾ M. A. Hannan,⁽¹⁾ M. Facchinelli,⁽¹⁾ and A. Massa,⁽¹⁾⁽⁴⁾⁽⁵⁾ *Fellow, IEEE*

⁽¹⁾ *ELEDIA Research Center (ELEDIA@Unitn - University of Trento)*

DICAM - Department of Civil, Environmental, and Mechanical Engineering

Via Mesiano 77, 38123 Trento - Italy

E-mail: {marco.salucci, lorenzo.poli, paolo.rocca, pietro.rosatti, mohammadabdul.hannan, mirko.facchinelli, andrea.massa}@unitn.it

Website: www.eledia.org/eledia-unitn

⁽²⁾ *ELEDIA Research Center (ELEDIA@XIDIAN - Xidian University)*

P.O. Box 191, No.2 South Tabai Road, 710071 Xi'an, Shaanxi Province - China

E-mail: paolo.rocca@xidian.edu.cn

Website: www.eledia.org/eledia-xidian

⁽³⁾ *Huawei Technologies Italia*

Centro Direzionale Milano2, Palazzo Verrocchio, 20054 Segrate - Italy

E-mail: claudio.massagrande1@huawei.com

⁽⁴⁾ *ELEDIA Research Center (ELEDIA@TSINGHUA - Tsinghua University)*

30 Shuangqing Rd, 100084 Haidian, Beijing - China

E-mail: andrea.massa@tsinghua.edu.cn

Website: www.eledia.org/eledia-tsinghua

⁽⁵⁾ *ELEDIA Research Center (ELEDIA@UESTC - UESTC)*

School of Electronic Engineering, Chengdu 611731 - China

E-mail: andrea.massa@uestc.edu.cn

Website: www.eledia.org/eledia-uestc

This work has been submitted to the IEEE for possible publication. Copyright may be transferred without notice, after which this version may no longer be accessible.

Spline-Shaped Microstrip Edge-Fed Antenna for 77 GHz Automotive Radar Systems

M. Salucci, L. Poli, P. Rocca, C. Massagrande, P. Rosatti, M. A. Hannan, M. Facchinelli, and A. Massa

Abstract

An innovative millimeter-wave (*mm*-wave) microstrip edge-fed antenna (*EFA*) for 77 GHz automotive radars is proposed. The radiator contour is modeled with a sinusoidal spline-shaped (*SS*) profile characterized by a reduced number of geometrical descriptors, but still able to guarantee a high flexibility in the modeling for fulfilling challenging user-defined requirements. The *SS-EFA* descriptors are effectively and efficiently optimized with a customized implementation of the System-by-Design (*SbD*) paradigm. The synthesized *EFA* layout, integrated within a linear arrangement of identical replicas to account for the integration into the real radar system, exhibits suitable impedance matching, isolation, polarization purity, and stability of the beam shaping/pointing within the target band $f_{\min} = 76$ [GHz] $\leq f \leq f_{\max} = 78$ [GHz]. The experimental assessment, carried out with a Compact Antenna Test Range (*CATR*) system on a printed circuit board (*PCB*)-manufactured prototype, assess the reliability of the outcomes from the full-wave (*FW*) simulations as well as the suitability of the synthesized *SS-EFA* for automotive radars.

Key words: Automotive Radar, *mm*-Waves, 77 [GHz] Bandwidth, Antenna Design, Spline, System-by-Design (*SbD*).

Nomenclature

<i>ACC</i>	Adaptive Cruise Control.
<i>AUT</i>	Antenna Under Test.
<i>BDD</i>	Beam Direction Deviation.
<i>CATR</i>	Compact Antenna Test Range.
<i>CFA</i>	Center-Fed Antenna.
<i>DoA</i>	Direction of Arrival.
<i>DoF</i>	Degree-of-Freedom.
<i>DT</i>	Digital Twin.
<i>EFA</i>	Edge-Fed Antenna.
<i>FF</i>	Far-Field.
<i>FMCW</i>	Frequency Modulated Continuous Wave.
<i>FW</i>	Full-Wave.
<i>LBE</i>	Learning-By-Examples.
<i>LHS</i>	Latin Hypercube Sampling.
<i>MC</i>	Mutual Coupling.
<i>MIMO</i>	Multiple-Input Multiple-Output.
<i>OK</i>	Ordinary Kriging.
<i>PCB</i>	Printed Circuit Board.
<i>PR</i>	Polarization Ratio.
<i>PSO</i>	Particle Swarm Optimizer.
<i>RS</i>	Resonant.
<i>SbD</i>	System-by-Design.
<i>SS</i>	Spline-Shaped.
<i>SSE</i>	Solution Space Exploration.
<i>SW</i>	Standing Wave.
<i>TW</i>	Travelling-Wave.
<i>VNA</i>	Vector Network Analyzer.

1 Introduction

Millimeter-wave (*mm-wave*) radars play an important role in many modern automotive applications ranging from active safety driver assistance systems to autonomous driving vehicles [1]-[3]. Thanks to the capability to measure the distance, the speed, and the direction of arrival (*DoA*) of multiple targets with low delays, they are frequently used for blind-spot detection, collision avoidance, and emergency brake assistance [4][5]. Moreover, automotive radars are a key technology for implementing active comfort systems featuring a high robustness against environmental conditions including high temperature, darkness, and bad weather. For instance, let us consider adaptive cruise control (*ACC*) systems that allow the vehicle to autonomously accelerate or brake or stop in case of traffic jam to relieve the driver of monotonous tasks.

In order to continuously sense and monitor the surrounding environment [1], multiple receive and transmit antennas/channels are used to implement frequency modulated continuous wave (*FMCW*) multiple-input multiple-output (*MIMO*) radars and 77 [GHz] solutions are particularly attractive because of the many advantages over systems operating at lower frequencies (e.g., 24 [GHz] band [1][6]). As a matter of fact, the exploitation of the 77 [GHz] band allows one to design smaller antennas with lower volume- and weight-related costs as well as to reach a higher spatial resolution and more precise *DoA* estimations [1].

As for the antenna implementation, different technological solutions have been explored in the last few years including Franklin antennas [6], series-fed microstrip arrays [7][8], comb-line arrays [9]-[12], lens antennas [13], dielectric resonator antennas [14], planar grid arrays [15], leaky-wave antennas [16], ceramic-filled cavity resonators [17], and substrate integrated waveguides (*SIWs*) [18]-[22]. Series-fed architectures are nowadays a mainstream choice because of the limited cost, the low profile, the light weight, and the simple manufacturing/integration in automotive systems. However, the feeding mechanism is more complex than that of traditional corporate feeding networks since all the (series-connected) radiating points must be in-phase excited to afford a well-shaped broadside radiation pattern. To address such an issue, both center-fed (*CFAs*) [23][24] and edge-fed (*EFAs*) [7] antennas have been studied. The former mitigates the beam tilting (or squint) due to the change of the electrical lengths between consecutive radiating locations at different frequencies within the working band, but they

may be unsuitable for a compact integration/connection to the driving pins of a *FMCW* radar micro-chip. Otherwise, *EFA*s can be more easily closely-packed in linear array arrangements by means of simpler routing connections [7]. However, the design of *EFA*s, which can be in turn implemented both as resonant (*RS*) and travelling-wave (*TW*) structures depending on the absence or presence of a matched load placed at the termination edge on the opposite of the feeding point [25], turns out to be more challenging because of the more difficult control of each excitation phase from a single feeding point located on one edge. Generally speaking, while *TW-EFA*s usually enable a more flexible beam shaping of the far-field (*FF*) pattern, they are also characterized by a larger beam direction deviation (*BDD*) with frequency and a lower radiation efficiency because of the energy dissipated in the terminating load [25].

This paper presents an innovative single-layer *RS* microstrip *EFA* for automotive radars in the 77 [GHz] band. Unlike state-of-art solutions, the contour of the radiating element is modeled as a spline-shaped (*SS*) profile [26]-[28]. Accordingly, arbitrarily-complex shapes can be yielded by acting on a limited set of geometric degrees-of-freedom (*DoFs*) to fulfil several challenging requirements on both bandwidth and radiation features. As a matter of fact, the flexibility of the proposed modeling approach enables an accurate control of the feeding phases within the operative band. Moreover, the non-uniformity of the radiator width allows one to optimize the elevation *FF* features including a lowering of the sidelobe level (*SLL*), which is beneficial for reducing both near range clutter from the road surface and the multi-path interferences. Moreover, to yield a robust/reliable design for a fruitful integration within *FMCW* automotive radars, the non-negligible material losses occurring in the *mm*-wave regime as well as the mutual coupling (*MC*) effects when integrating the antenna in the radar system composed by a linear arrangement of identical elements are taken into account by recurring to a full-wave (*FW*) modelling of the structure at hand.

Owing to the complexity of the synthesis problem at hand, the System-by-Design (*SbD*) [29]-[32] paradigm has been applied to solve the arising global optimization problem with a high computational efficiency. More in detail, the design of the *SS RS-EFA* (shortly in the following *SS-EFA*) has been carried out by means of a customized version of the *PSO-OK/C* method [29] based on a “low dimension” representation of the solution space and relying on the “collab-

oration” between a Solution Space Exploration (*SSE*) functional block based on evolutionary operators [33]-[35] and a Learning-By-Examples (*LBE*)-based digital twin (*DT*) of the *FW* simulator aimed at outputting fast predictions of the electromagnetic (*EM*) performance of each trial guess solution generated by the *SSE* [36].

The paper is organized as follows. Section 2 describes the *SS-EFA* geometry and it provides some theoretical insights on its electromagnetic (*EM*) working principle. The design requirements and the *SbD* procedure for the synthesis of the antenna layout are detailed in Sect. 3. Section 4 presents selected results from the *FW*-based numerical assessment of the performance of the optimized radiator along with the experimental validation of a *SS-EFA* prototype realized on a printed circuit board (*PCB*) and measured on a custom *mm*-wave Compact Antenna Test Range (*CATR*) system. Finally, some conclusions are drawn (Sect. 5).

2 *SS-EFA* Layout and *EM* Working Principle

The layout of the *SS-EFA* is shown in Fig. 1. The antenna lies on the (x, y) plane and it is printed on a ground-backed Rogers *RO3003TM* high frequency ceramic-filled composite substrate with relative permittivity and loss tangent equal to $\varepsilon_r = 3.0$ and $\tan \delta = 1.0 \times 10^{-3}$, respectively, of thickness $h = 0.127$ [mm] (i.e., $h = 5$ [mil]). To take into account all non-idealities/losses occurring in the *mm*-wave band, both metallizations on the top (i.e., the radiator) and the bottom (i.e., the ground plane) layers are modeled as copper with conductivity $\sigma = 2.5 \times 10^7$ [S/m], thickness $\tau = 25 \times 10^{-6}$ [m], and roughness $\rho = 1.3 \times 10^{-6}$ [m].

The antenna is fed from the bottom edge with a tapered microstrip feeding line of length l_1 , having controllable starting, w_1 , and ending, w_2 , widths to yield a proper 50 [Ω] impedance matching over the complete working band. As for the shape of the radiator, which is connected to the feeding line, an innovative non-uniform *SS* profile is adopted [26]-[28] since (i) there is the possibility to model complex geometries for fitting multiple and sometimes contrasting requirements on both bandwidth and far-field (*FF*) features with a reduced set of properly-tuned *DoFs*; (ii) the absence of sharp edges is a recipe to mitigate the fringing effects that enhance the *MC* between the adjacent elements of the final radar layout [27]. More in detail, Bézier spline basis functions [27], with $C = 37$ control points, $\underline{P} = \{P_c = (x_c, y_c); c = 1, \dots, C\}$ (Fig. 1),

are adopted to shape the contour of the *SS-EFA*.

The spline radiator is terminated on the opposite side of the feeding point with an open circuit (i.e., no matched load) so that a resonant behavior is yielded by exciting a standing wave (*SW*) within the microstrip structure (Fig. 2). As a matter of fact, the radiation of *EM* energy originates from the bending corners of the *SS-EFA* that, in turn, correspond to the fixed positions of the *SW* maxima (Fig. 2). To afford the desired resonating behavior, the surface current in such locations must be tuned in-phase so that the *FF* radiated contributions constructively add in the antenna broadside direction [i.e., $(\theta_0, \varphi_0) = (0, 0)$ [deg] - Fig. 1]. Towards this end, the electrical length of each o -th ($o = 1, \dots, O$; $O \triangleq \frac{C-1}{3} \rightarrow O = 12$) intermediate spline segment, α_o , must be properly designed so that the current, injected from the feeding point and flowing up to the open circuit, is equally-phased at each radiating location (Fig. 2) despite the single-point edge-feeding mechanism.

It is also worth pointing out that thanks to the non-uniform width of the *SS* metallization (e.g., $\gamma_1 \neq \gamma_2$ - Fig. 3), it is possible to excite a tapered current distribution within the *EFA* to perform beam shaping for obtaining a lower *SLL* with respect to a uniform-width profile. Such a *FF* feature is highly desirable in automotive applications since it reduces the interferences from both the asphalt and the sky, thus leading to a more robust and reliable target detection/location and *DoA* estimation.

As for the *FF* half-power beamwidth (*HPBW*), which affects the angular resolution of the automotive radar along the elevation plane, it is controlled by the overall length of the *SS* radiator. Indeed, longer structures exhibit narrower *HPBW*s (e.g., $\beta_2 > \beta_1 \rightarrow HPBW|_{\beta_2} < HPBW|_{\beta_1}$ - Fig. 3) and vice-versa, because of the different aperture size of the equivalent linear array.

In order to guarantee geometric/electric symmetry by also keeping low the number of problem descriptors, only one half of the spline curve (i.e., $\{P_c; c = 1, \dots, 19\}$ - Fig. 1) is optimized, while the coordinates of the second half of the control points (i.e., $\{P_c; c = 20, \dots, C\}$ - Fig. 1) are automatically derived with a mirroring operation with respect to the horizontal axis (i.e., x -axis - Fig. 1). Enforcing such a symmetry allows one to also yield a lower *BDD* and a higher similarity of the left/right side-lobes on the vertical plane (i.e., $\varphi = 90$ [deg] - Fig. 1).

Finally, it is important to point out that despite the unconventional and non-uniform shaping

of the radiating element, the *SS-EFA* radiates a linearly polarized field along the horizontal direction with a high polarization purity. As a matter of fact, the surface current density distributions excited within each pair of adjacent spline branches (e.g., $\underline{J}_1 = J_{1,x}\hat{x} + J_{1,y}\hat{y}$ and $\underline{J}_2 = J_{2,x}\hat{x} + J_{2,y}\hat{y}$ - Fig. 4) exhibit in-phase x -components (e.g., $J_{1,x}$ and $J_{2,x}$ - Fig. 4) and out-of-phase y -components (e.g., $J_{1,y}$ and $J_{2,y}$ - Fig. 4) so that, while the x -components constructively sum, the y ones cancel out and the *EM* source turns out to be x -polarized.

3 Design Process

The *SS-EFA* has been synthesized to provide a suitable matching so that $|S_{11}(f)| \leq S_{11}^{th}$ ($S_{11}^{th} = -10$ [dB]) within the frequency range $\Delta f = [f_{\min}, f_{\max}]$ [20], f_{\min} and f_{\max} being the minimum ($f_{\min} = 76$ [GHz]) and the maximum ($f_{\max} = 78$ [GHz]) working frequency, respectively. Concerning the radiation features, the *SLL*, the *HPBW*, and the *BDD* on the vertical plane have been required to comply with the following requirements: $SLL(f) \leq SLL^{th}$ ($SLL^{th} = -15$ [dB]), $HPBW(f) \leq HPBW^{th}$ ($HPBW^{th} = 18$ [deg]), and $BDD(f) \leq BDD^{th}$ ($BDD^{th} = 2$ [deg])⁽¹⁾. Furthermore, the polarization ratio (*PR*) is required to be $PR(f) \geq PR^{th}$ ($PR^{th} = 20$ [dB])⁽²⁾. For the sake of clarity, all design objectives/targets are reported in Tab. I.

To yield a robust design and to enable a reliable prediction of the *EM* behavior of the elementary radiator when integrated in an automotive radar system⁽³⁾, it has been synthesized not alone, but within a linear arrangement of $N = 5$ identical half-wavelength ($W = \frac{\lambda_0}{2} = 1.95 \times 10^{-3}$ [m], λ_0 being the free-space wavelength at the central frequency $f_0 = 77$ [GHz]) spaced *SS-EFAs* (Fig. 5), which has been modeled with a *FW* finite model. More specifically, the synthesis has been aimed at optimizing all performance indexes for the central embedded element, while the surrounding $(N - 1)$ replicas have been terminated on 50 [Ω] matched loads (Fig. 5).

Owing to the computational complexity of the synthesis problem at hand, the design has been

⁽¹⁾The *BDD* is defined as $BDD(f) = |\theta_{\max}(f)|$, where $\theta_{\max}(f) = \arg \left\{ \max_{\theta} \left[G(f, \theta, \varphi) \right]_{\varphi=90[\text{deg}]} \right\}$, $G(f, \theta, \varphi)_{\varphi=90[\text{deg}]}$ being the gain pattern function in the vertical (elevation) plane of the antenna (Fig. 1).

⁽²⁾The *PR* is defined as $PR(f) = \left| \frac{E_x(f, \theta=0)}{E_y(f, \theta=0)} \right|$, $E_{x/y}$ being the x/y -components of the *FF* electric field, respectively.

⁽³⁾*FMCW* multiple-input multiple-output (*MIMO*) automotive radars are generally implemented as properly-spaced arrangements of both transmitting and receiving elementary radiators connected to a single driving chip [1][37][38].

efficiently carried out within the *SbD* framework [29]-[32]. According to such an optimization paradigm, a “smart” representation of the solution space has been considered by setting the following $K = 20$ descriptors $\underline{\chi} = \{\chi_k; k = 1, \dots, K\}$ where $\chi_k = l_k$ ($k = 1, \dots, T; T = 11$) and $\chi_k = w_{k-T}$ ($k = T + 1, \dots, T + U; U = 9$) (Fig. 1) instead of using the coordinates of the control points of the spline contour (i.e., $K = 2 \times C \rightarrow K = 74$). The synthesis problem has been then reformulated as a minimization one by defining the following cost function

$$\Phi(\underline{\chi}) = \sum_{\Psi \in \mathcal{T}} \Phi_{\Psi} \{\underline{\chi}\}, \quad (1)$$

where $\mathcal{T} = \{S_{11}; SLL; HPBW; BDD; PR\}$ and $\Phi_{\Psi} \{\underline{\chi}\}$ is given by

$$\Phi_{\Psi} \{\underline{\chi}\} = \frac{1}{Q} \sum_{q=1}^Q \mathcal{H} \left\{ \frac{\Psi(f_q | \underline{\chi}) - \Psi^{th}}{|\Psi^{th}|} \right\} \quad (2)$$

being $\Psi(f_q | \underline{\chi}) \in \{S_{11}(f_q | \underline{\chi}); SLL(f_q | \underline{\chi}); HPBW(f_q | \underline{\chi}); BDD(f_q | \underline{\chi}); -PR(f_q | \underline{\chi})\}$, $\Psi^{th} \in \{S_{11}^{th}; SLL^{th}; HPBW^{th}; BDD^{th}; -PR^{th}\}$, while $\mathcal{H}\{\xi\} = \xi$ if $\xi \geq 0$ and $\mathcal{H}\{\xi\} = 0$, otherwise. Moreover, the frequency band Δf has been uniformly sampled into $Q = 41$ points, $\{f_q = f_{\min} + (q - 1) \frac{(f_{\max} - f_{\min})}{(Q - 1)}; q = 1, \dots, Q\}$, for constraining the fulfilment of the requirements in the whole bandwidth.

The minimization of (1) has been carried out with a properly customized version of the *PSO-OK/C SbD* method [29] leveraging on the “collaboration” between the *SSE* functional block relying on the Particle Swarm Optimization (*PSO*) operators [35] and a fast *DT* based on the Ordinary Kriging (*OK*) *LBE* technique [36]. The meta-level control parameters of the *PSO* have been set according to the literature guidelines [29]: $V = 10$ (V being the swarm size), $I = 200$ (I being the maximum number of iterations), $\omega = 0.4$ (ω being the inertial weight), and $\mathcal{C}_1 = \mathcal{C}_2 = 2.0$ (\mathcal{C}_1 and \mathcal{C}_2 being the social and the cognitive acceleration coefficient, respectively).

As for the *OK* prediction model, the fast surrogate of the *FW* simulator has been trained with $S_0 = 100$ training samples generated *off-line* according to the Latin Hypercube Sampling (*LHS*) strategy [29], while $S_{upd} = 200$ “reinforcement training” *FW* simulations have been performed *on-line* by the *PSO-OK/C* to adaptively enhance the *DT* accuracy during the iterative minimiza-

tion of (1).

The solution, $\underline{\chi}^{(opt)}$, outputted by the *SbD* at the convergence [i.e., $\Phi(\underline{\chi}^{(opt)}) = 0$] that fulfils all the user-defined requirements, as it can be inferred in Sect. 4.1, is reported in Tab. II, while the *CAD* model of the corresponding *SS-EFA* layout is shown in Fig. 5, the total length of the radiator being equal to $L = l_1 + 2 \times (b + l_2 + l_3 + l_5 + l_6 + l_8 + l_9 + l_{11}) \rightarrow L = 18.9 \times 10^{-3}$ [m] since $b = 3 \times 10^{-3}$ [m] is a fixed offset from the bottom and the top edges of the substrate (Fig. 1).

It is worthwhile to point out that the time saving Δt [$\Delta t \triangleq \frac{(V \times I) - (S_0 + S_{upd})}{(V \times I)}$] enabled here by the *SbD* strategy [29] with respect to a standard optimization that exclusively relies on iterated *FW* calls (i.e., $V \times I$) [34] amounts to $\Delta t = 85\%$.

4 Performance Assessment

The goal of this section is twofold. On the one hand, to present the results of a careful assessment of the *FW*-simulated *EM* features of the synthesized *SS-EFA* (Sect. 4.1). On the other hand, to show the outcomes from the experimental validation, carried out on a *PCB*-manufactured prototype, to confirm the *FW* simulations (Sect. 4.2) towards the use of the proposed *mm*-wave radiator in automotive radar applications.

4.1 Numerical Assessment

Figure 6 shows the behavior of the reflection coefficient of the central ($n = 1$) embedded element within the linear arrangement of $N = 5$ identical *SS-EFAs* simulated by means of the Ansys *HFSS FW* solver [39]. As it can be inferred, the antenna correctly resonates within the operative band being $|S_{11}(f)| \leq -11.6$ [dB], $f \in \Delta f$. Moreover, the optimized *SS-EFA* provides a suitable inter-element isolation as indicated by the magnitude of the scattering coefficients [i.e., $|S_{n1}(f)| \leq -22.6$ [dB] ($n = 2, \dots, N$)].

As for the *FF* features of the *SbD*-layout, the plots in Fig. 7(a) show that the requirements on both the *SLL* and the *HPBW* are fulfilled since $SLL(f) \leq -15.3$ [dB] and $HPBW(f) \leq 17.5$ [deg], $f \in \Delta f$. Moreover, the synthesized radiator turns out to be fully-compliant in terms of

beam pointing stability regardless of the adopted edge feeding mechanism as confirmed by the BDD values (i.e., $BDD \leq 1.5$ [deg]) in Fig. 7(b).

On the other hand, it should be very interesting for the readers to observe that the arising $SS-EFA$ structure radiates a linearly (horizontal) polarized field with high polarization purity despite its smooth/non-uniform profile (Fig. 1). Indeed, it turns out that $PR(f) \geq 21$ [dB], $f \in \Delta f$ [Fig. 7(b)] as a consequence of the distribution of the surface current (Fig. 8) that follows the theoretically-expected configuration sketched in Fig. 4. An overall x -polarized source is excited in correspondence with each radiating location of the resonant structure shown in Fig. 10 where the near-field (NF) distribution of the magnitude of the electric field, $|\mathbf{E}(x, y; f_0)|$, computed on a $(5W \times L)$ -sized plane at height $z = \frac{\lambda_0}{20}$ from the $SS-EFA$, is reported. This latter plot highlights the resonant behavior of the synthesized structure, the field being maximum at fixed and equally-spaced positions. As expected, such maxima, which correspond to those of the SW excited within the structure, arise on the bends of the spline contour and they generate in-phase radiation contributions that result in a suitable beam shaping and a pointing stability within the working band Δf as confirmed by the simulated FF pattern at $f = f_{\min}$, $f = f_0$, and $f = f_{\max}$ in Fig. 9.

4.2 Experimental Validation

A prototype of the $SS-EFA$ has been fabricated through PCB manufacturing on a substrate of size 70×70 [mm] (Fig. 11). The bottom ground plane has been stacked on a 1 [mm]-thick $FR-4$ layer to enhance the mechanical robustness and rigidity of the antenna under test (AUT). Moreover, four holes, 3.5 [mm] in diameter, have been drilled at the corners of a square of side 48.5 [mm] to fix the AUT on the measurement support by means of plastic screws [Fig. 11(a) and Fig. 12(a)]. The central radiator ($n = 1$) has been fed by using a Rosemberger $01K80A-40ML5$ connector installed without soldering at the bottom edge of the AUT substrate [Fig. 12(a)]. The neighboring SS elements (i.e., $n = 2, \dots, N$) have been terminated on $MCR1$ compact thick film chip resistors (series 0402) acting as matched loads. Moreover, the active and the dummy radiators as well as the feeding line have been surrounded by a double set of interleaved vias to suppress the insurgence of undesired surface currents due to the electrically-

large dimension of the *PCB* [Fig. 11(b)].

The measurement set-up [Figs. 12(b)-12(c)] has been composed by a *mm*-wave *CATR* system within an Asysol anechoic chamber (Fig. 13) suitable for antenna measurements up to 170 [GHz].

Figure 14 shows the *SS-EFA* gain patterns measured along the $\varphi = 90$ [deg]-cut at the minimum [$f = f_{\min}$ - Fig. 14(a)], the central [$f = f_0$ - Fig. 14(b)], and the maximum [$f = f_{\max}$ - Fig. 14(c)] operating frequencies. As it can be observed, the *FF* pattern of the prototype well matches the simulated one yielded by modeling the layout of Fig. 11 with the *Ansys HFSS FW* simulator. More specifically, there is a very good agreement in both the main lobe region and the first left/right sidelobes, while a slight beam pointing deviation between simulated and measured patterns ($\Delta\theta \approx 3$ [deg], $\Delta\theta \triangleq \theta_{\max}^{sim} - \theta_{\max}^{meas}$) occurs at the maximum frequency [$f = f_{\max}$ - Fig. 14(c)]. This is probably due to both prototype manufacturing inaccuracies and measurement tolerances whose impact is certainly significant in the *mm*-wave regime.

Finally, the *FW*-predicted *SLL* performance is assessed by the measurements since $SLL^{meas} \leq -14.5$ [dB], $f \in \Delta f$ (Fig. 14).

5 Conclusions

A novel radiating element for 77 GHz automotive radars has been proposed that relies on a spline-based modeling to yield a high geometric flexibility with a reduced number of *DoFs*, while enabling the fitting of the several contrasting requirements on bandwidth and *FF* features. The synthesized layout, which has been efficiently obtained by means of a customized *SbD* approach, provides a proper input impedance matching, a high isolation, a suitable *SLL/HPBW* as well as a high polarization purity and a stable beam pointing over frequency regardless of the edge-feeding mechanism. The experimental assessment, carried out in a *CATR mm*-wave system on a *PCB*-manufactured prototype, has verified the *FW*-predicted radiation features over the operative band.

Acknowledgements

This work benefited from the networking activities carried out within the Project "EMvisioning - Cyber-Physical Electromagnetic Vision: Context-Aware Electromagnetic Sensing and Smart Reaction" (Grant no. 2017HZJXSZ) funded by the Italian Ministry of Education, University, and Research within the PRIN2017 Program (CUP: E64I19002530001), the Project "MAN-TLES - Cloaking Metasurfaces for a new Generation of Intelligent Antenna Systems" (Grant no. 2017BHFZKH) funded by the Italian Ministry of Education, University, and Research within the PRIN2017 Program (CUP: E64I19000560001), the Project "MITIGO - Mitigazione dei rischi naturali per la sicurezza e la mobilit  nelle aree montane del Mezzogiorno" (Grant no. ARS01_00964) funded by the Italian Ministry of Education, University, and Research within the PON R&I 2014-2020 Program (CUP: B64I20000450005), and the Project "SPEED" (Grant No. 6721001) funded by National Science Foundation of China under the Chang-Jiang Visiting Professorship Program. A. Massa wishes to thank E. Vico for her never-ending inspiration, support, guidance, and help.

References

- [1] J. Hasch, E. Topak, R. Schnabel, T. Zwick, R. Weigel, and C. Waldschmidt, "Millimeter-wave technology for automotive radar sensors in the 77 GHz frequency band," *IEEE Trans. Microw. Theory Techn.*, vol. 60, no. 3, pp. 845-860, Mar. 2012.
- [2] D. Kissinger, *Millimeter-Wave Receiver Concepts for 77 GHz Automotive Radar in Silicon-Germanium Technology*. New York: Springer-Verlag, 2012.
- [3] M. Kim and S. Kim, "Design and fabrication of 77-GHz radar absorbing materials using frequency-selective surfaces for autonomous vehicles application," *IEEE Microw. Wireless Compon. Lett.*, vol. 29, no. 12, pp. 779-782, Dec. 2019.
- [4] J. Overdevest, F. Jansen, F. Uysal, and A. Yarovoy, "Doppler influence on waveform orthogonality in 79 GHz MIMO phase-coded automotive radar," *IEEE Trans. Veh. Technol.*, vol. 69, no. 1, pp. 16-25, Jan. 2020.

- [5] E. Klinefelter and J. A. Nanzer, "Automotive velocity sensing using millimeter-wave interferometric radar," *IEEE Trans Microw. Theory Techn.*, vol. 69, no. 1, pp. 1096-1104, Jan. 2021.
- [6] C. Kuo, C. Lin, and J. Sun, "Modified microstrip Franklin array antenna for automotive short-range radar application in blind spot information system," *IEEE Antennas Wireless Propag. Lett.*, vol. 16, pp. 1731-1734, 2017.
- [7] J. Xu, W. Hong, H. Zhang, G. Wang, Y. Yu, and Z. H. Jiang, "An array antenna for both long and medium-range 77 GHz automotive radar applications," *IEEE Trans. Antennas Propag.*, vol. 65, no. 12, pp. 7207-7216, Dec. 2017.
- [8] Y. Q. Guo, Y. M. Pan, and S. Y. Zheng, "Design of series-fed, single-layer, and wideband millimeter-wave microstrip arrays," *IEEE Trans. Antennas Propag.*, vol. 68, no. 10, pp. 7017-7026, Oct. 2020.
- [9] M. Mosalanejad, I. Ocket, C. Soens, and G. A. E. Vandenbosch, "Wideband compact comb-line antenna array for 79 GHz automotive radar applications," *IEEE Antennas Wireless Propag. Lett.*, vol. 17, no. 9, pp. 1580-1583, Sep. 2018.
- [10] S. Afoakwa and Y. Jung, "Wideband microstrip comb-line linear array antenna using stubbed-element technique for high sidelobe suppression," *IEEE Trans. Antennas Propag.*, vol. 65, no. 10, pp. 5190-5199, Oct. 2017.
- [11] Y. Hayashi, K. Sakakibara, M. Nanjo, S. Sugawa, N. Kikuma, and H. Hirayama, "Millimeter-wave microstrip comb-line antenna using reflection-canceling slit structure," *IEEE Trans. Antennas Propag.*, vol. 59, no. 2, pp. 398-406, Feb. 2011.
- [12] J. Lee, J. M. Lee, K. C. Hwang, D. Seo, D. Shin, and C. Lee, "Capacitively coupled microstrip comb-line array antennas for millimeter-wave applications," *IEEE Antennas Wireless Propag. Lett.*, vol. 19, no. 8, pp. 1336-1339, Aug. 2020.
- [13] P. Hallbjorner, Z. He, S. Bruce, and S. Cheng, "Low-profile 77-GHz lens antenna with array feeder," *IEEE Antennas Wireless Propag. Lett.*, vol. 11, pp. 205-207, 2012.

- [14] W. M. Abdel-Wahab, D. Busuioc, and S. Safavi-Naeini, "Millimeter-wave high radiation efficiency planar waveguide series-fed dielectric resonator antenna (DRA) array: Analysis, design, and measurements," *IEEE Trans. Antennas Propag.*, vol. 59, no. 8, pp. 2834-2843, Aug. 2011.
- [15] E. Arnieri, F. Greco, L. Boccia, and G. Amendola, "A reduced size planar grid array antenna for automotive radar sensors," *IEEE Antennas Wireless Propag. Lett.*, vol. 17, no. 12, pp. 2389-2393, Dec. 2018.
- [16] M. Ettorre, R. Sauleau, L. Le Coq, and F. Bodereau, "Single-folded leaky-wave antennas for automotive radars at 77 GHz," *IEEE Antennas Wireless Propag. Lett.*, vol. 9, pp. 859-862, 2010.
- [17] F. Bauer and W. Menzel, "A 79-GHz planar antenna array using ceramic-filled cavity resonators in LTCC," *IEEE Antennas Wireless Propag. Lett.*, vol. 12, pp. 910-913, 2013.
- [18] S. Cheng, H. Yousef, and H. Kratz, "79 GHz slot antennas based on substrate integrated waveguides (SIW) in a flexible printed circuit board," *IEEE Trans. Antennas Propag.*, vol. 57, no. 1, pp. 64-71, Jan. 2009.
- [19] A. Dewantari, J. Kim, I. Scherbatko, and M. H. Ka, "A sidelobe level reduction method for mm-wave substrate integrated waveguide slot array antenna," *IEEE Antennas Wireless Propag. Lett.*, vol. 18, no. 8, pp. 1557-1561, Aug. 2019.
- [20] Y. Yu, W. Hong, H. Zhang, J. Xu, and Z. H. Jiang, "Optimization and implementation of SIW slot array for both medium- and long-range 77 GHz automotive radar application," *IEEE Trans. Antennas Propag.*, vol. 66, no. 7, pp. 3769-3774, Jul. 2018.
- [21] M. S. Abdallah, Y. Wang, W. M. Abdel-Wahab, and S. Safavi-Naeini, "Design, and optimization of SIW center-fed series rectangular dielectric resonator antenna array with 45° linear polarization," *IEEE Trans. Antennas Propag.*, vol. 66, no. 1, pp. 23-31, Jan. 2018.
- [22] J. Xu, Z. N. Chen, and X. Qing, "CPW center-fed single-layer SIW slot antenna array for automotive radars," *IEEE Trans. Antennas Propag.*, vol. 62, no. 9, pp. 4528-4536, Sep. 2014.

- [23] R. Chopra and G. Kumar, "Series-fed binomial microstrip arrays for extremely low side-lobe level," *IEEE Trans. Antenna Propag.*, vol. 67, no. 6, pp. 4275-4279, Jun. 2019.
- [24] N. Boskovic, B. Jokanovic, M. Radovanovic, and N. S. Doncov, "Novel Ku-band series-fed patch antenna array with enhanced impedance and radiation bandwidth," *IEEE Trans. Antennas Propag.*, vol. 66, no. 12, pp. 7041-7048, Dec. 2018.
- [25] H. Yi, L. Li, J. Han, and Y. Shi, "Traveling-wave series-fed patch array antenna using novel reflection-canceling elements for flexible beam," *IEEE Access*, vol. 7, pp. 111466-111476, Aug. 2019.
- [26] M. Salucci, C. Castlunger, D. Marcantonio, G. Oliveri, F. Robol, P. Rosatti, L. Tosato, F. Zardi, and A. Massa, "High density interconnect microstrip patch antenna for 5G base stations with integrated filtering performance," *Technologies*, vol. 6, no. 2, p. 45, Apr. 2018.
- [27] M. Salucci, F. Robol, N. Anselmi, M. A. Hannan, P. Rocca, G. Oliveri, M. Donelli, and A. Massa, "S-Band spline-shaped aperture-stacked patch antenna for air traffic control applications," *IEEE Trans. Antennas Propag.*, vol. 66, no. 8, pp. 4292-4297, Aug. 2018.
- [28] M. Salucci, L. Tenuti, G. Gottardi, A. Hannan, and A. Massa, "A System-by-Design method for efficient linear array miniaturization through low-complexity isotropic lenses," *Electron. Lett.*, vol. 55, no. 8, pp. 433-434, Apr. 2019.
- [29] A. Massa and M. Salucci, "On the design of complex *EM* devices and systems through the System-by-Design paradigm - A framework for dealing with the computational complexity," *IEEE Trans. Antennas Propag.*, vol. 70, no. 2, pp. 1328-1343, Feb. 2022.
- [30] M. Salucci, G. Oliveri, M. A. Hannan, and A. Massa, "System-by-Design paradigm-based synthesis of complex systems: The case of spline-contoured 3D radomes," *IEEE Antennas Propag. Mag.*, vol. 64, no. 1, pp. 72-83, Feb. 2022.
- [31] G. Oliveri, M. Salucci, N. Anselmi, and A. Massa, "Multi-scale system-by-design synthesis of printed WAIMs for waveguide array enhancement," *IEEE J. Multiscale Multiphys. Comput. Techn.*, vol. 2, pp. 84-96, Jun. 2017.

- [32] G. Oliveri, A. Gelmini, A. Polo, N. Anselmi, and A. Massa, "System-by-design multi-scale synthesis of task-oriented reflectarrays," *IEEE Trans. Antennas Propag.*, vol. 68, no. 4, pp. 2867-2882, Apr. 2020.
- [33] S. Goudos, *Emerging Evolutionary Algorithms for Antennas and Wireless Communications*. Stevenage: SciTech Publishing Inc., 2021.
- [34] S. K. Goudos, C. Kalialakis, and R. Mittra, "Evolutionary algorithms applied to antennas and propagation: A review of state of the art," *Int. J. Antennas Propag.*, vol. 2016, pp. 1-12, Jan. 2016.
- [35] P. Rocca, M. Benedetti, M. Donelli, D. Franceschini, and A. Massa, "Evolutionary optimization as applied to inverse scattering problems," *Inverse Problems*, vol. 24, no. 12, pp. 1-41, 2009.
- [36] A. Massa, G. Oliveri, M. Salucci, N. Anselmi, and P. Rocca, "Learning-by-examples techniques as applied to electromagnetics," *J. Electromagn. Waves Appl.*, vol. 32, no. 4, pp. 516-541, 2018.
- [37] K. Tan, T. Yin, H. Ruan, S. Balon, and X. Chen, "Learning approach to FMCW radar target classification with feature extraction from wave physics," *IEEE Trans. Antennas Propag.*, DOI: 10.1109/TAP.2022.3175716.
- [38] W. A. Ahmad, M. Kucharski, A. Ergintav, H. J. Ng, and D. Kissinger, "A planar differential wide fan-beam antenna array architecture: Modular high-gain array for 79-GHz multiple-input, multiple-output radar applications," *IEEE Antennas Propag. Mag.*, vol. 63, no. 4, pp. 21-32, Aug. 2021.
- [39] ANSYS Electromagnetics Suite - HFSS (2021). ANSYS, Inc.

FIGURE CAPTIONS

- **Figure 1.** *SS-EFA Design* - Sketch of the antenna geometry with its geometrical descriptors.
- **Figure 2.** *SS-EFA Working Principle* - Pictorial representation of the radiation mechanism.
- **Figure 3.** *SS-EFA Working Principle* - Sketch of two non-uniform width ($\gamma_1 \neq \gamma_2$) and different length ($\beta_1 \neq \beta_2$) *SS-EFAs*.
- **Figure 4.** *SS-EFA Working Principle* - Pictorial representation of the behavior of the surface current density.
- **Figure 5.** *Numerical Assessment* ($N = 5$) - Screenshot of the *SbD*-synthesized optimal *SS-EFA* radiator layout embedded within a $N = 5$ linear array of identical $\frac{\lambda_0}{2}$ -spaced replicas.
- **Figure 6.** *Numerical Assessment* ($N = 5$) - Magnitude of the reflection coefficient, $|S_{11}(f)|$ ($n = 1$), and of the scattering coefficients, $|S_{n1}(f)|$ ($n = 2, \dots, N$), of the central embedded element ($n = 1$) versus the frequency f ($f \in \Delta f$) for the linear arrangement in Fig. 5.
- **Figure 7.** *Numerical Assessment* ($N = 5, n = 1, \varphi = 90$ [deg]) - Behavior of (a) *SLL* and *HPBW* and (b) *BDD* and *PR* versus the frequency f ($f \in \Delta f$).
- **Figure 8.** *Numerical Assessment* ($N = 5, n = 1$) - Screenshot of the simulated surface current density at $f = f_0$.
- **Figure 9.** *Numerical Assessment* ($N = 5, n = 1, \varphi = 90$ [deg]) - Embedded gain pattern at $f = f_{\min}$, $f = f_0$, and $f = f_{\max}$.
- **Figure 10.** *Numerical Assessment* ($N = 5, n = 1$) - Screenshot of the magnitude of the total electric field, $|\mathbf{E}(x, y; f_0)|$, computed over a plane parallel to the (x, y) plane far $z = \frac{\lambda_0}{20}$ from the *SS-EFA* surface, at $f = f_0$.

- **Figure 11.** *Experimental Assessment* - Picture of (a) the *SS-EFA* prototype and (b) a zoom on the radiating part.
- **Figure 12.** *Experimental Assessment* - Picture of (a) the *AUT*, (b) the *CATR* positioner, and (c) the whole measurement setup.
- **Figure 13.** *Experimental Assessment* - Sketch of the measurement scenario.
- **Figure 14.** *Experimental Assessment* ($N = 5$, $n = 1$, $\varphi = 90$ [deg]) - Comparison between simulated and measured embedded element patterns at (a) $f = f_{\min}$, (b) $f = f_0$, and (c) $f = f_{\max}$.

TABLE CAPTIONS

- **Table I.** Radar antenna requirements.
- **Table II.** Values of the descriptors of the *SbD*-synthesized *SS-EFA* layout.

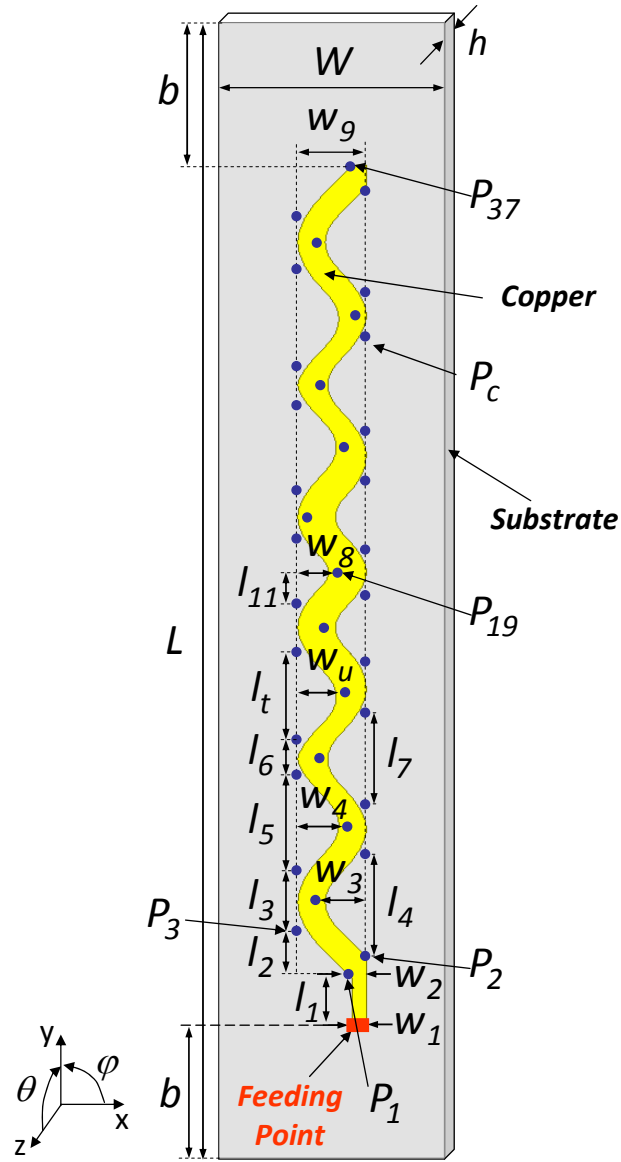


Fig. 1 - M. Salucci et al., "Spline-Shaped Microstrip Edge-Fed Antenna ..."

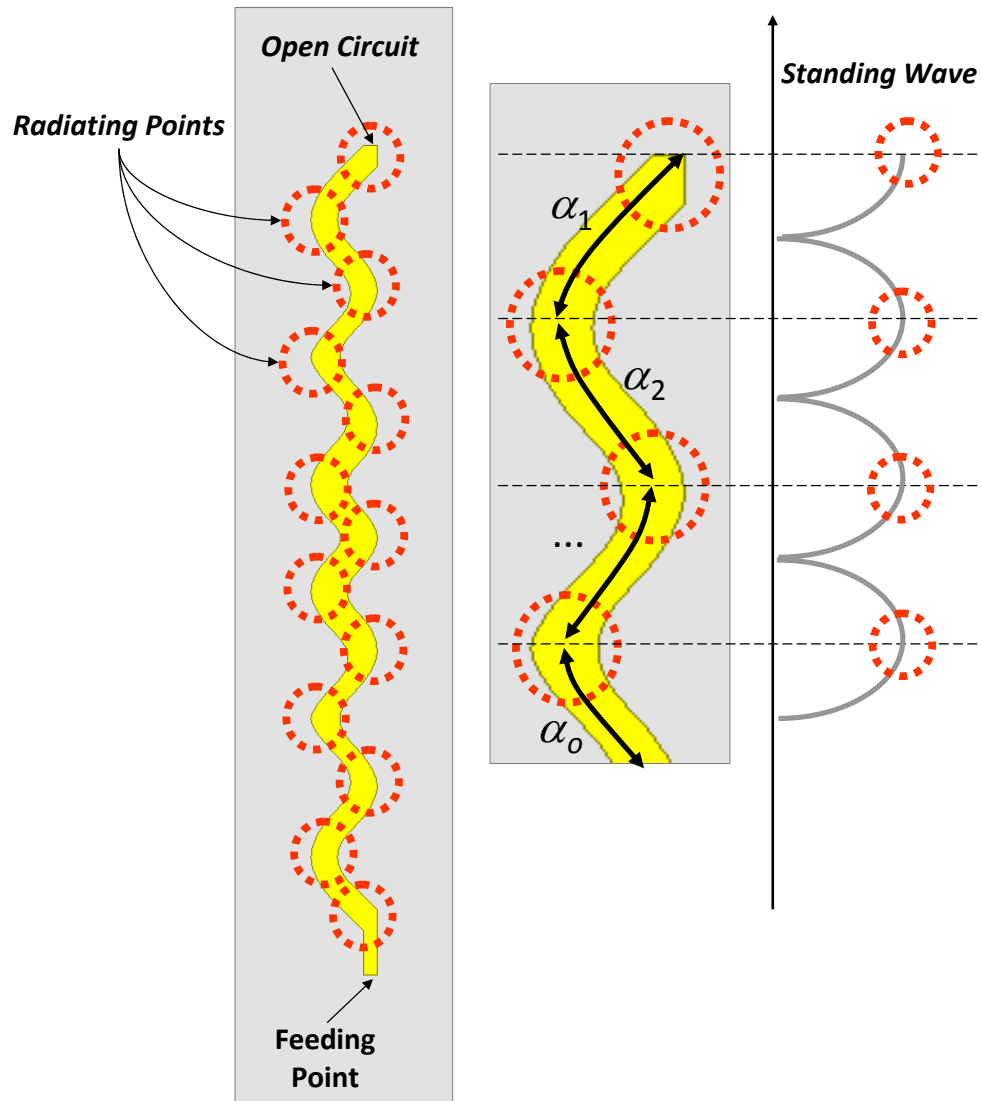


Fig. 2 - M. Salucci et al., “Spline-Shaped Microstrip Edge-Fed Antenna ...”

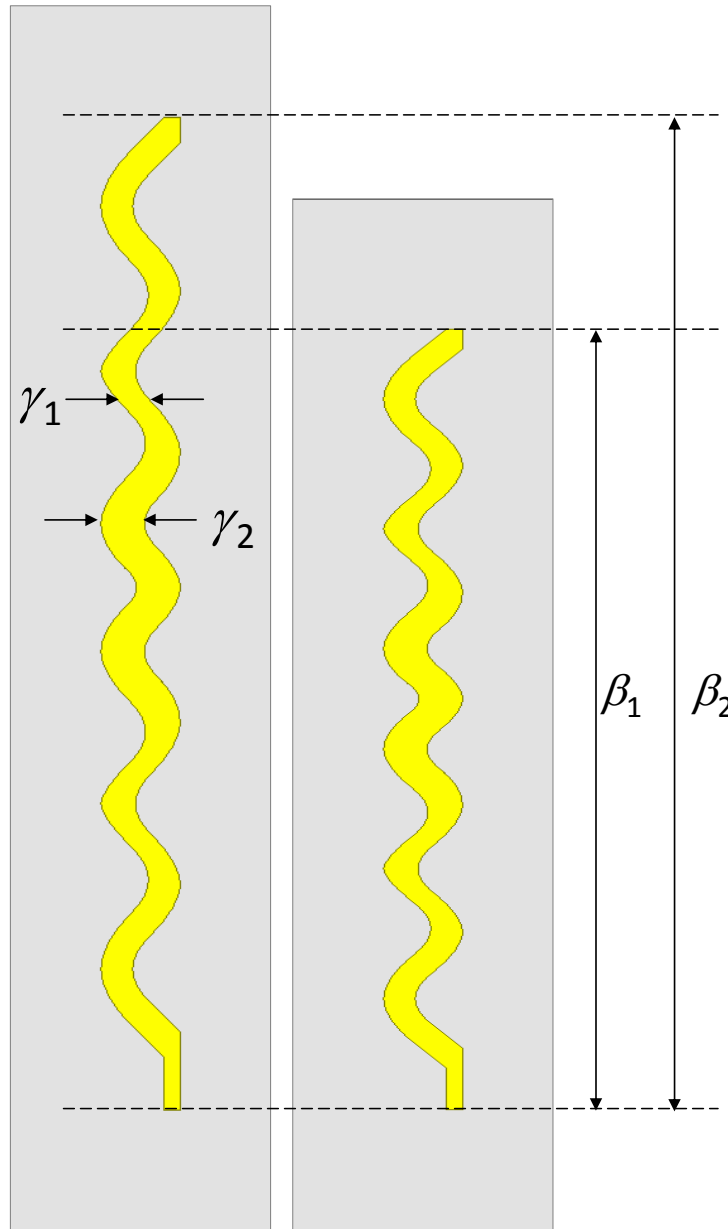


Fig. 3 - M. Salucci et *al.*, “Spline-Shaped Microstrip Edge-Fed Antenna ...”

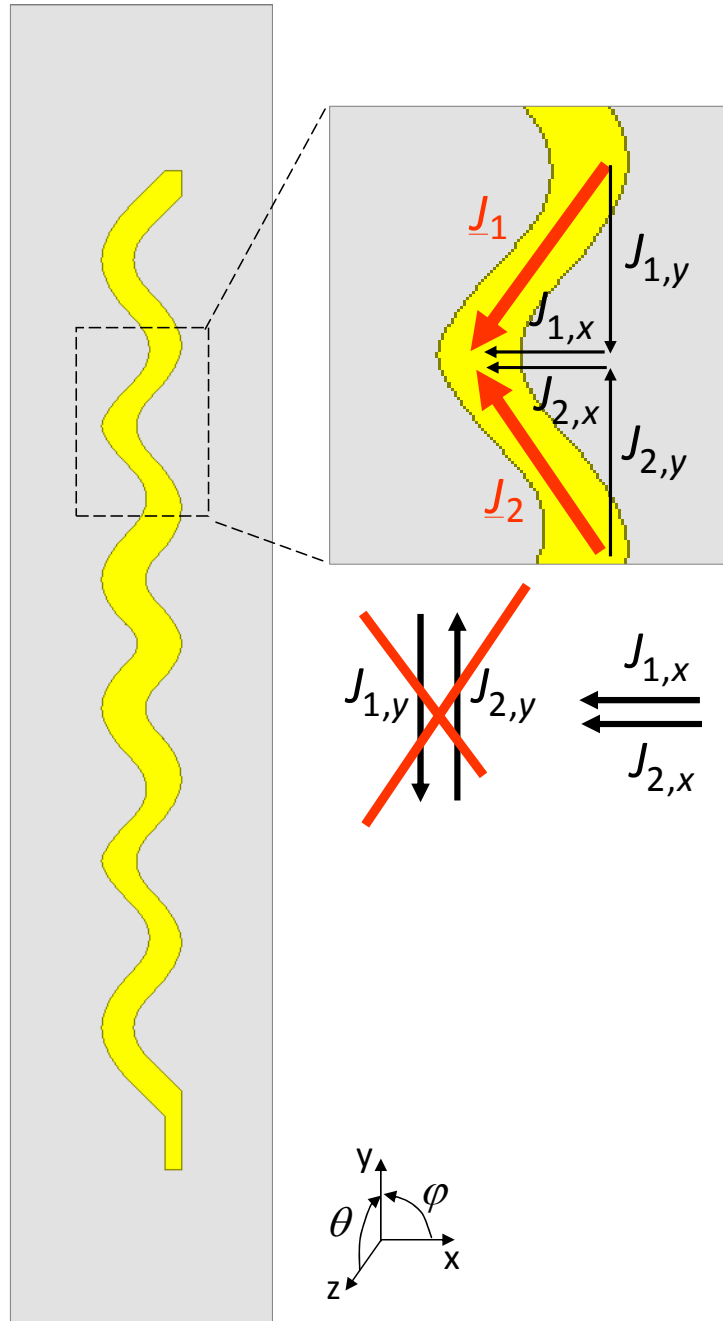


Fig. 4 - M. Salucci et *al.*, “Spline-Shaped Microstrip Edge-Fed Antenna ...”

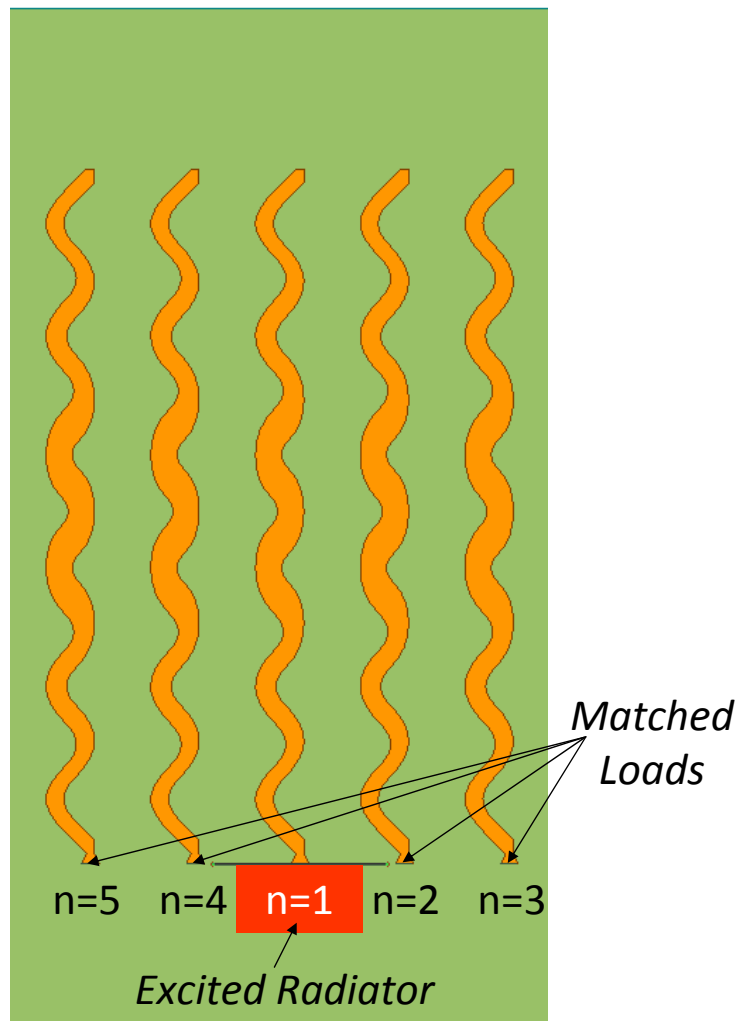


Fig. 5 - M. Salucci et *al.*, “Spline-Shaped Microstrip Edge-Fed Antenna ...”

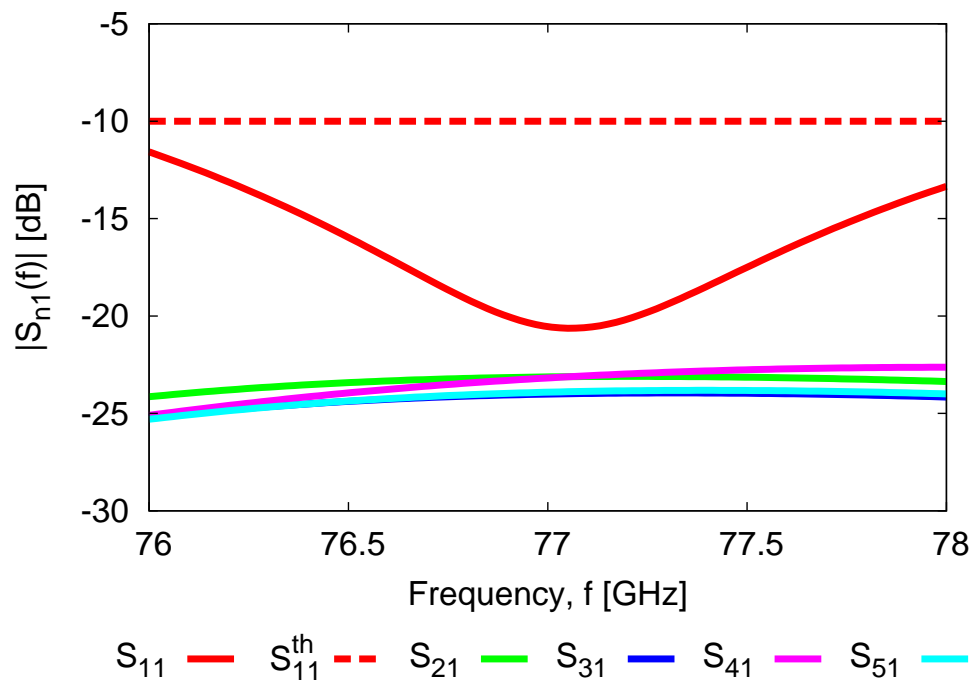


Fig. 6 - M. Salucci et *al.*, “Spline-Shaped Microstrip Edge-Fed Antenna ...”

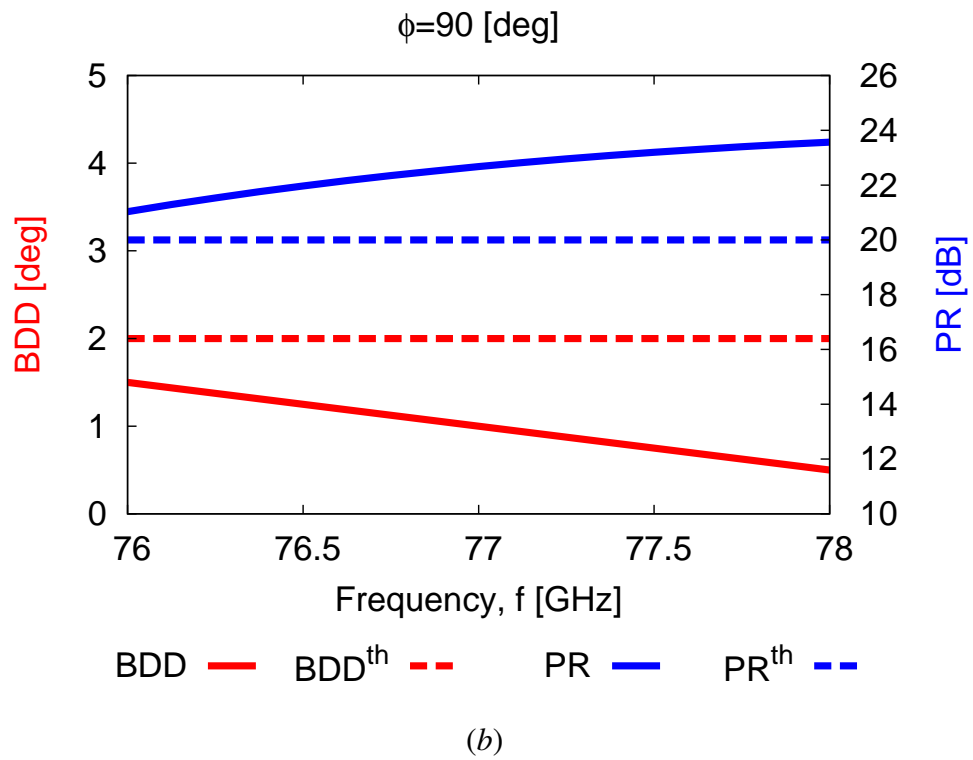
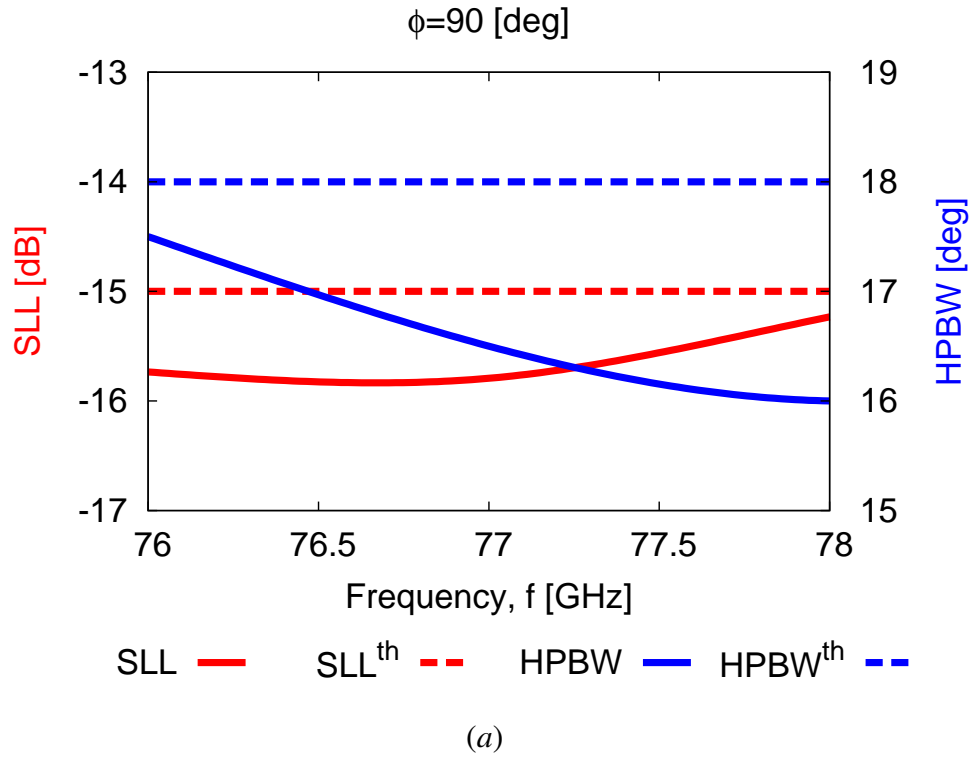


Fig. 7 - M. Salucci et *al.*, “Spline-Shaped Microstrip Edge-Fed Antenna ...”

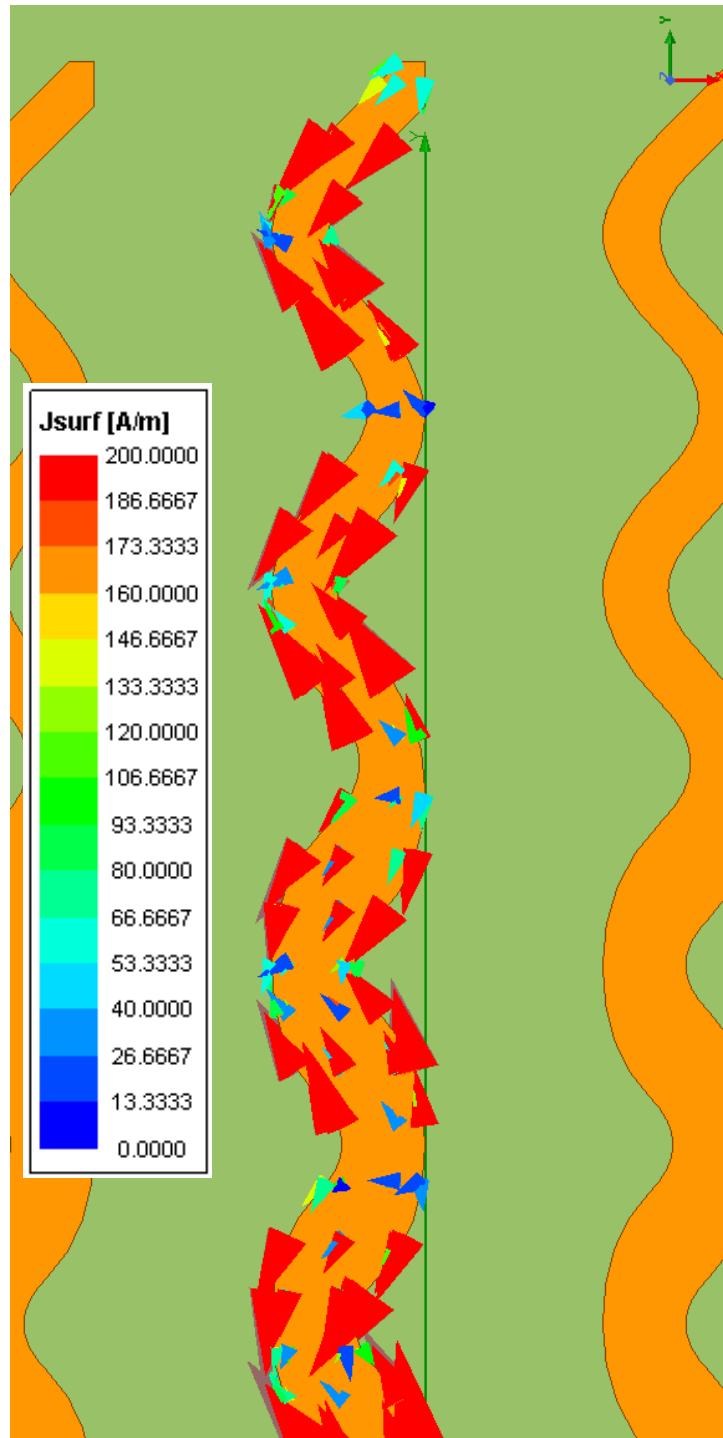


Fig. 8 - M. Salucci et al., “Spline-Shaped Microstrip Edge-Fed Antenna ...”

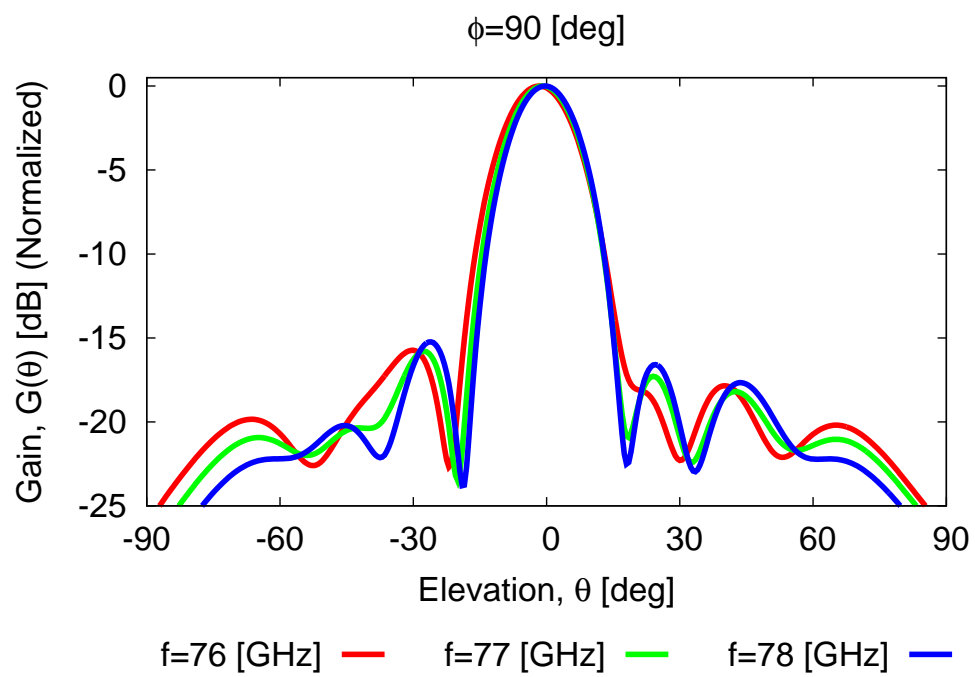


Fig. 9 - M. Salucci et *al.*, “Spline-Shaped Microstrip Edge-Fed Antenna ...”

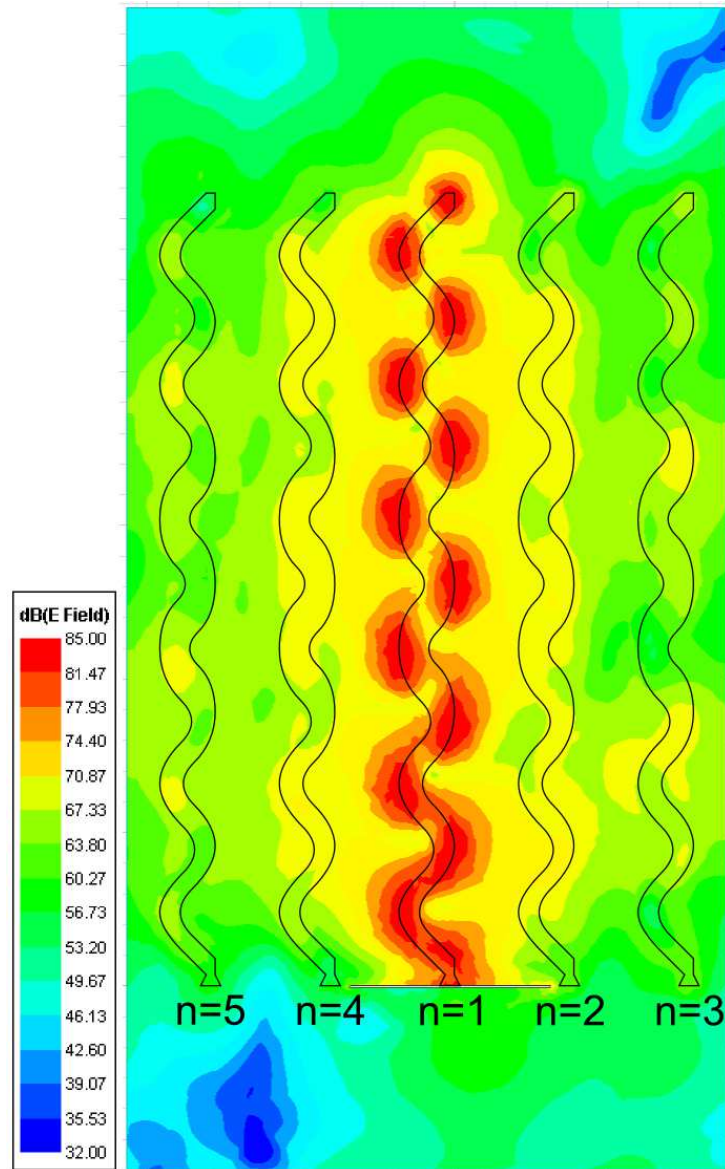
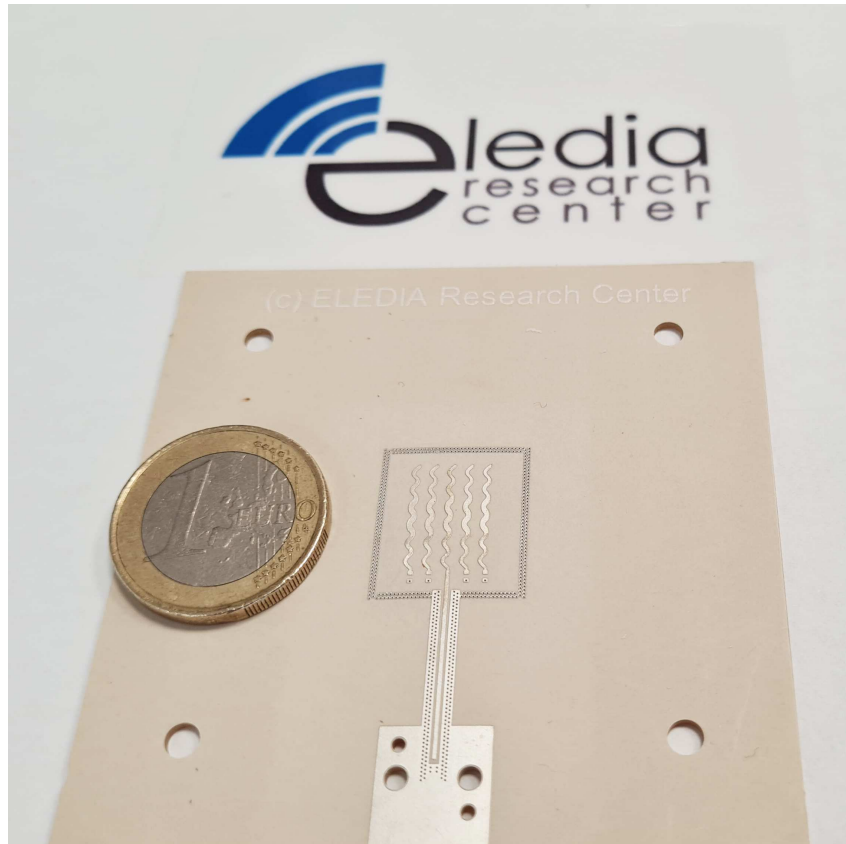
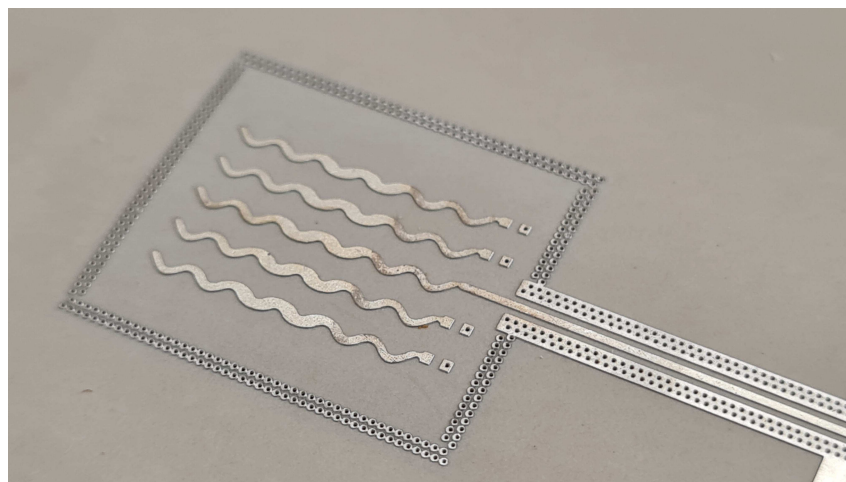


Fig. 10 - M. Salucci et *al.*, “Spline-Shaped Microstrip Edge-Fed Antenna ...”

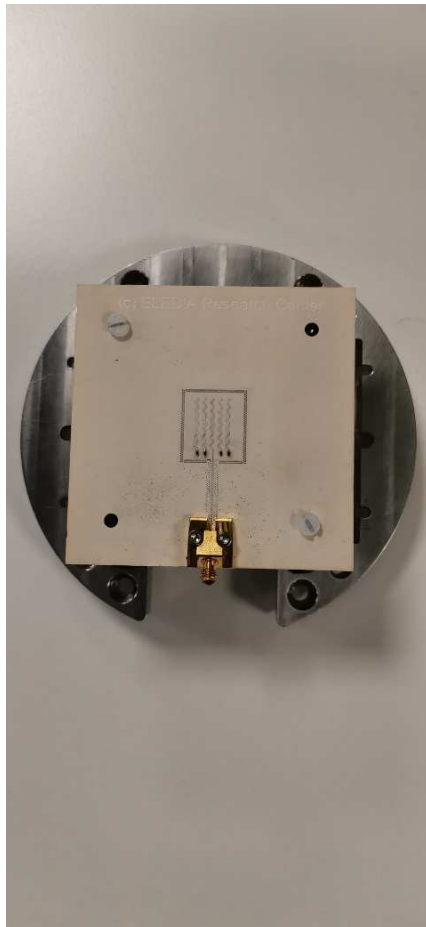


(a)

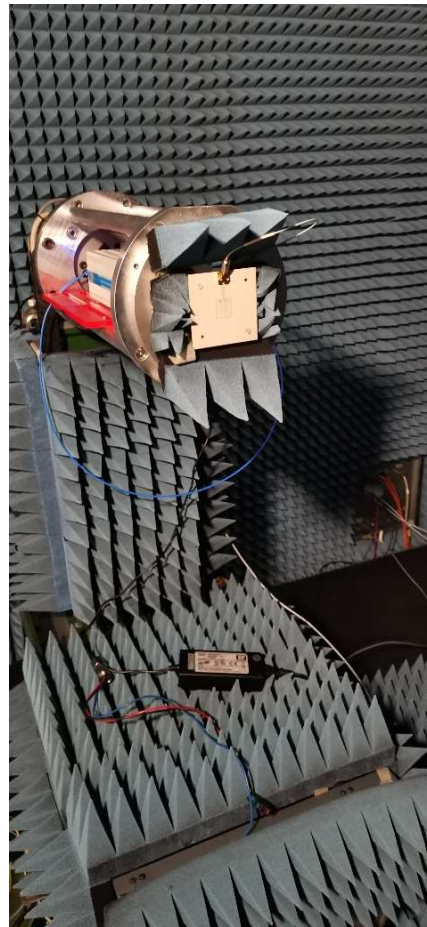


(b)

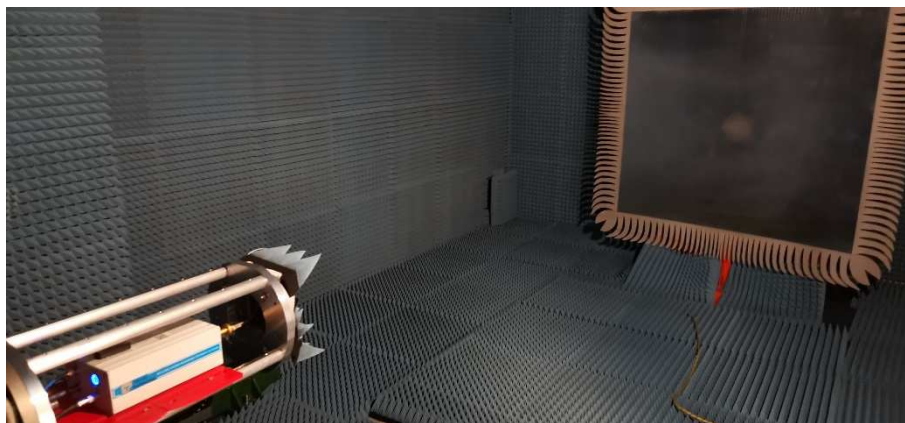
Fig. 11 - M. Salucci et *al.*, “Spline-Shaped Microstrip Edge-Fed Antenna ...”



(a)



(b)



(c)

Fig. 12 - M. Salucci et *al.*, “Spline-Shaped Microstrip Edge-Fed Antenna ...”

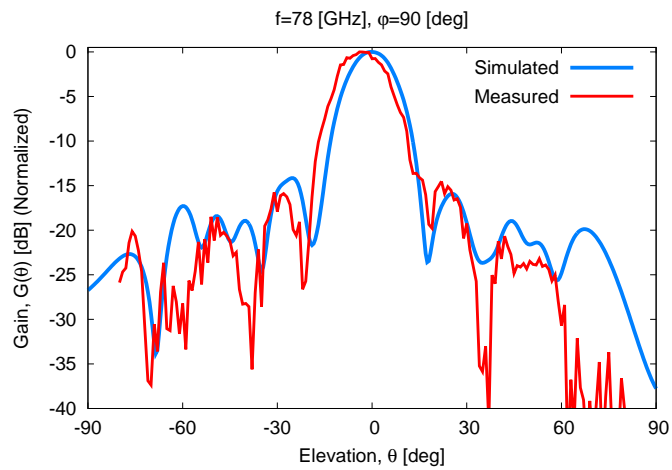
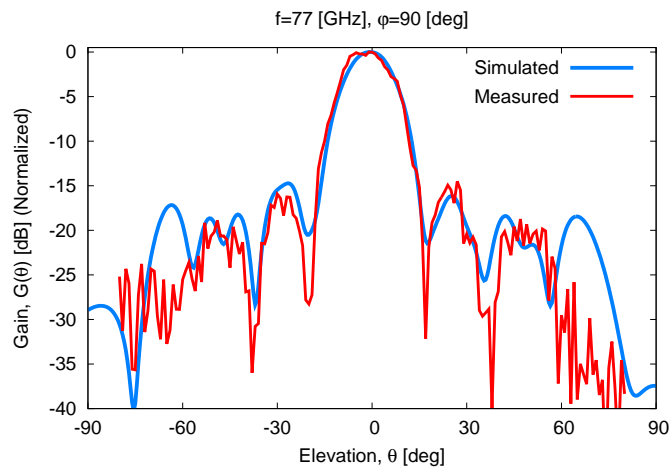
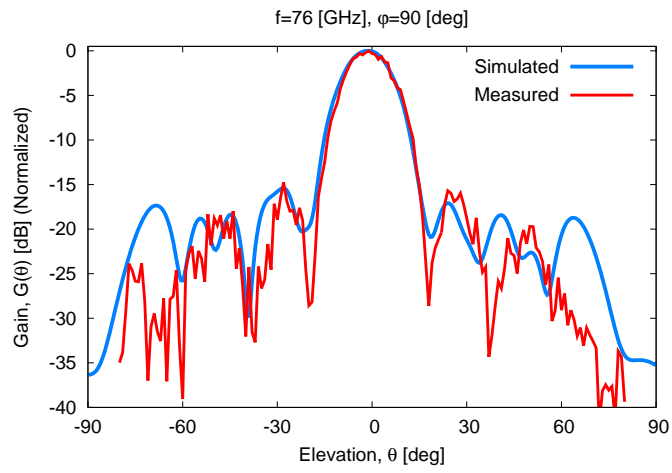


Fig. 14 - M. Salucci et al., “Spline-Shaped Microstrip Edge-Fed Antenna ...”

<i>Feature</i>	<i>Requirement</i>
Operating Band	$f \in [f_{\min}, f_{\max}] = [76, 78] \text{ [GHz]}$
Reflection Coefficient	$S_{11} \leq S_{11}^{th} = -10 \text{ [dB]}$
Sidelobe Level	$SLL \leq SLL^{th} = -15 \text{ [dB]}$
Half-Power Beamwidth	$HPBW \leq HPBW^{th} = 18 \text{ [deg]}$
Beam Direction Deviation	$BDD \leq BDD^{th} = 2 \text{ [deg]}$
Polarization Ratio	$PR \geq PR^{th} = 20 \text{ [dB]}$

Tab. I - M. Salucci et al., “Spline-Shaped Microstrip Edge-Fed Antenna ...”

Geometrical Descriptors [m]			
w_1	3.26×10^{-4}	l_2	7.57×10^{-4}
w_2	1.46×10^{-4}	l_3	5.27×10^{-4}
w_3	7.57×10^{-4}	l_4	1.51×10^{-3}
w_4	7.57×10^{-4}	l_5	1.51×10^{-3}
w_5	6.90×10^{-4}	l_6	6.47×10^{-4}
w_6	6.90×10^{-4}	l_7	1.38×10^{-3}
w_7	5.52×10^{-4}	l_8	1.38×10^{-3}
w_8	5.52×10^{-4}	l_9	1.00×10^{-3}
w_9	9.03×10^{-4}	l_{10}	1.10×10^{-3}
l_1	1.80×10^{-4}	l_{11}	5.22×10^{-4}

Tab. II - M. Salucci et *al.*, “Spline-Shaped Microstrip Edge-Fed Antenna ...”